APPLIED AND ENVIRONMENTAL MICROBIOLOGY, Jan. 2009, p. 83–92 Vol. 75, No. 1
0099-2240/09/$08.00+0 doi:10.1128/AEM.01799-08
Copyright © 2009, American Society for Microbiology. All Rights Reserved.

In Silico *Geobacter sulfurreducens* Metabolism and Its Representation in Reactive Transport Models[▽]

E. L. King,[1] K. Tuncay,[2] P. Ortoleva,[3] and C. Meile[1]*

Department of Marine Sciences, University of Georgia, Athens, Georgia 30602[1]; Department of Civil Engineering, Middle East Technical University NCC, Kalkanli, Guzelyurt TRNC, Mersin 10, Turkey[2]; and Department of Chemistry, Indiana University Bloomington, Bloomington, Indiana 47405[3]

Received 4 August 2008/Accepted 3 November 2008

Microbial activity governs elemental cycling and the transformation of many anthropogenic substances in aqueous environments. Through the development of a dynamic cell model of the well-characterized, versatile, and abundant *Geobacter sulfurreducens*, we showed that a kinetic representation of key components of cell metabolism matched microbial growth dynamics observed in chemostat experiments under various environmental conditions and led to results similar to those from a comprehensive flux balance model. Coupling the kinetic cell model to its environment by expressing substrate uptake rates depending on intra- and extracellular substrate concentrations, two-dimensional reactive transport simulations of an aquifer were performed. They illustrated that a proper representation of growth efficiency as a function of substrate availability is a determining factor for the spatial distribution of microbial populations in a porous medium. It was shown that simplified model representations of microbial dynamics in the subsurface that only depended on extracellular conditions could be derived by properly parameterizing emerging properties of the kinetic cell model.

Microbes control the breakdown of organic matter in low-temperature subsurface environments. Their activities affect the physicochemical nature of the local environment, drive elemental cycling, and determine the fate of many contaminants (9, 49). Effects can be direct (for example, by altering the local chemical composition through the utilization of substrates and terminal electron acceptors for energy production and growth or cometabolism) or indirect (for example, by affecting the presence and the chemical nature of solid iron phases, which determines sorption and coprecipitation of transition metals and contaminants) (4, 6, 17, 51). In addition, hydrological factors such as groundwater flow patterns and velocities can impact cell metabolism through nutrient delivery, with possible feedbacks through bioclogging (46).

To predict how bacteria regulate their activity and grow in situ, it is necessary to quantitatively understand the complex and dynamic interactions between the numerous concurrent biogeochemical processes involved, which requires the use of mathematical models. While subsurface reactive transport models generally contain a comparatively sound description of the physical transport processes (3, 34), they often do not explicitly account for the dynamics of microbial populations that mitigate the majority of biogeochemical processes (18, 48). When included, microbes are typically represented as functional groups, with growth dynamics depending linearly on substrate availability or following Monod kinetics (27, 38, 44), an approach that has been successful in describing geochemical contaminant plume dynamics (7). However, lacking a realistic representation of microbial metabolism, such models are limited in their capability of reflecting microbial dynamics and forecasting the response to changing environmental conditions, which restricts their predictive power at the macroscale and their usefulness, for example, in the assessment of conditions that optimize in situ bioremediation (22).

With the advent of genome sequencing, over the last decade, the biological revolution has led to the characterization of cellular metabolic networks and to the development of mathematical models at the cell scale (41), ranging from descriptions of network topology (20, 45) to constraint-based models for different organisms (13, 33, 42) and fully kinetic approaches (e.g., see references 2, 30, and 50). Integration of such models of environmentally important groups of bacteria in reactive transport simulations would clearly benefit forecasting biogeochemical responses to changing macroscopic conditions. The gammaproteobacteria *Geobacteraceae* constitute such an abundant and environmentally important group in both pristine and contaminated sediment environments (22). *Geobacter* species are metabolically diverse and can grow with numerous electron donors and acceptors, including acetate or H_2, and Fe(III), fumarate, or malate, respectively (8, 23). They have been shown to be enriched when Fe(III) reduction is promoted in a petroleum-contaminated sandy aquifer (39) and to mediate the reduction of U(VI) to U(IV) (25), converting the soluble form to the insoluble form and effectively removing the uranium from the groundwater (51). *Geobacter* shapes biogeochemical cycling directly through its metabolic activity, as well as indirectly, such as via the effect of iron (hydr)oxide reduction on the motility of sorbed trace metals and on pH.

In this study, we present a kinetic cell model of *Geobacter sulfurreducens* metabolism and its application in the simulation of a subsurface contaminant plume with the following goals: (i) to assess the kinetic description of central cellular metabolism and the growth efficiencies emerging under a range of substrate conditions by comparing them to observational data; (ii) to quantify the sensitivity of model results to the parameter-

* Corresponding author. Mailing address: Department of Marine Sciences, University of Georgia, Athens, GA 30602-3636. Phone: (706) 542-6549. Fax: (706) 542-5888. E-mail: cmeile@uga.edu.
▽ Published ahead of print on 14 November 2008.

Downloaded from http://aem.asm.org/ on July 24, 2020 at ORTA DOGU TEKNIK UNIVERSITESI

ization of the enzymatic reactions of the tricarboxylic acid (TCA) cycle and gluconeogenesis considered here; (iii) to compare and contrast different cell model approaches; (iv) to introduce a coupling approach between cell metabolic expressions and macroscopic reactive transport models; and (v) to assess the potential and the limits of macroscopic models that parameterize microscopic intracellular processes. Our cell model is validated against growth efficiencies obtained in chemostat experiments (12) and is compared to the flux balance (FB) model developed by Mahadevan et al. (26) who—based on an extensive genome analysis—used a constraint-based modeling approach to estimate steady-state intracellular fluxes and metabolite exchange with the environment. To assess the role of microbial dynamics in the environment, an acetate plume is studied in a heterogeneous porous medium, for which simulations with a full coupling between the environment and the cell model are contrasted with several simplified parameterizations, including commonly used Monod approximations.

MATERIALS AND METHODS

Dynamic cell model. The dynamic cell model was implemented in the kinetic cell model simulator Karyote (31), which divides metabolic reactions into those that occur at equilibrium (fast reactions) or at a finite rate (slow reactions). For example, a single-substrate isomerization reaction occurs by the fast formation of an enzyme-substrate complex ($S + E \overset{Q_f}{\leftrightarrow} ES$) followed by a slow dissociation ($ES \overset{k,kQ_s}{\longleftrightarrow} P + E$), where Q_f is the equilibrium constant for the fast reaction and k and kQ_s are the backward and forward rate constants for the slow reactions, respectively.

Under typical natural subsurface conditions, the oxidation of acetate in *Geobacter*—initially activated through the combined actions of acetate kinase (AK; EC 2.7.2.1) and phosphate acetyltransferase (10)—is coupled to the reduction of Fe(III) (24), which is believed to take place on the extracellular membrane (21). Thus, the kinetic cell model encompassed the uptake of acetate and its incorporation into biomass via gluconeogenesis or its complete oxidation in the TCA cycle (10, 14) (Fig. 1). Two compartments—one extracellular and the other intracellular—were considered. The extracellular compartment accounted for species concentrations that represented environmental conditions, while the intracellular one accounted for enzymatic reactions and resource allocation in cellular metabolism. Reactions were formulated using mass action kinetics:

$$\frac{dc_i}{dt} = \sum_l \nu_{li}\left(-k_l \prod_{j=1}^{N_p} c_j^{\nu_{lj}} + Q_l k_l \prod_{j=1}^{N_r} c_j^{-\nu_{lj}} \right) \quad (1)$$

where c_i is the concentration of species i, Q_l is the equilibrium constant, k_l is the backward rate constant for reaction l, ν_l denotes stoichiometric coefficients, and N_p and N_r are the number of products and number of reactants, respectively. Model parameters were derived from the literature and are given in Table A1. As the literature rarely contains enzymatic forward and reverse rate constants, model parameters were typically derived from enzyme turnover numbers, specific activities, and substrate affinities. Details of the procedures and sources for model parameterization are given in the Appendix.

Sensitivity analysis. The effect of the uncertainties in reaction rate parameters k and Q on the predicted growth efficiencies was quantified over a range of extracellular acetate concentrations by performing cell model simulations with perturbed parameter sets. Parameters k and Q were selected at random from a normal distribution centered at the literature-derived base value with a 5.7% standard deviation. Sensitivity coefficients, s_j, which constitute a measure of the response of the growth efficiency to a change in parameter j, were determined via a multivariate linear regression using

$$g_{\text{eff}}^i - g_{\text{eff}}^{\text{base}} = \sum_j s_j (p_j^i - p_j^{\text{base}})/\text{p}_j^{\text{base}} \quad (2)$$

where g_{eff} is the growth efficiency, i indicates the i^{th} random realization, base denotes the baseline simulation, and j identifies the parameter p_j, set here to the backward and forward rate constants (k, kQ) and equilibrium constants for fast reactions (Q_f; see Appendix).

Cellular energy dynamics. Cellular energy dynamics were accounted for through reactions utilizing and producing AMP, ADP, and ATP. In addition to the energy used in the phosphorylation of acetate and pyruvate (Fig. 1, reactions 2 and 9), ATP is also produced through the reactions of the TCA cycle and consumed through cell growth and reactions required for cell maintenance according to the following equation:

$$\frac{d\text{ATP}}{dt} = 0.5 \cdot R_{\text{TCA}} \cdot \delta_T - (a \cdot R_g + R_m) \cdot \delta_D \quad (3)$$

where R_{TCA} is the overall rate of the TCA cycle, in which every acetate that cycles through will ultimately produce 0.5 ATP molecules (26). R_g is the growth rate, and a converts the rate of growth into ATP usage and is set to 19 mol_{ATP} $\text{mol}_{\text{acetate}}^{-1}$. It was based on ATP usage in the growth reaction of Mahadevan et al. (26) and modified to exclude the growth reactions explicitly accounted for in the reaction network (Fig. 1). R_m represents ATP consumption for cell maintenance, set to 0.45 mmol_{ATP} per gram of dry weight (g_{dw}) h^{-1} (26), and δ_T and δ_D reflect the presence of ATP and ADP, respectively (1 if present, 0 otherwise). ATP, ADP, and AMP values were further constrained through a fast exchange of ATP + AMP = 2ADP that mimicked the balance between adenosine phosphates not modeled at the process level (29). Levels of other substances involved in intracellular energy regulation, such as NAD-NADH, NADP-NADPH, CO_2, and phosphates (P_i, PP), were assumed to be constant (Fig. 1).

Acetate uptake. Acetate uptake rates for the kinetic cell model were formulated using the four-state model for a facilitated diffusion carrier kinetics (2), in which the flux of acetate across the cell membrane, J_{ac} (mol liter^{-1} s^{-1}), is described by

$$J_{\text{ac}} = \frac{A \cdot h \cdot (C_{\text{in}} - C_{\text{out}})}{V} \quad (4)$$

where C_{in} and C_{out} are the intracellular and extracellular concentrations (mol liter^{-1}) of acetate, respectively, V is the cellular volume (liters), A is the cell surface area (dm^2), and h (dm s^{-1}) describes the transport of acetate across the cell membrane, as described by the following equation:

$$h = \frac{(K_t)^2 Y}{K_t(K_t + C_{\text{in}} + C_{\text{out}}) + \alpha C_{\text{in}} C_{\text{out}}} \quad (5)$$

where K_t is a half-saturation constant (10 μM) (12), Y is the maximum exchange of acetate (dm s^{-1}), and the symmetry index α is set to 0 for symmetric cross-membrane transport of acetate. Cell area was calculated based on *G. sulfurreducens* cell size (37), assuming a cylindrical shape. Maximum acetate exchange ($Y = 1.20 \times 10^{-4}$ dm s^{-1}) was set to match the results from *Geobacter* chemostat experiments (12).

Growth efficiency was calculated from the acetate uptake flux and the flux of acetate through phosphoenolpyruvate (PEP) with the following equation: $g_{\text{eff}} = \alpha_{\text{pep}}\beta/J_{\text{ac}}$, where α_{pep} is the molar concentration of PEP produced per unit of time and β describes the grams of dry weight of biomass produced per mole of PEP created. β was calculated from a growth efficiency of 4.4×10^{-3} g_{dw} $\text{mmol}_{\text{acetate}}^{-1}$ at a cell-specific growth rate, μ, of 0.06 h^{-1} and an acetate flux to gluconeogenesis (Q) of 0.30 $\text{mol}_{\text{acetate}}$ $\text{g}_{\text{dw}}^{-1}$ h^{-1} (26). Taking into account the 2-to-3 acetate-to-PEP carbon ratio, $\beta = 2\mu/3Q = 0.3$ g_{dw} $\text{mmol}_{\text{PEP}}^{-1}$.

Flux balance model. Cellular metabolic rates under a range of acetate uptake fluxes were calculated using the FB model of *G. sulfurreducens* metabolism by Mahadevan et al. (26), which estimated intracellular fluxes and metabolite exchange with the environment for a given acetate uptake. The metabolic fluxes (reaction rates f) were sought, where for a network described by a stoichiometric matrix S,

$$S \cdot f = 0 \quad (6)$$

implying steady state. The fluxes were determined via optimizing a specific objective function, which is subjected to physiological constraints on the magnitude of the fluxes, as follows: lower bound $\leq f \leq$ upper bound. Maximization of biomass production rate was used as an objective function, which had been shown to lead to results in agreement with experimental data (26). The FB model was implemented in MATLAB, and growth efficiencies were calculated from the ratio of growth rate (f_{growth}) and acetate uptake (f_{ac}) as $g_{\text{eff}} = f_{\text{growth}}/f_{\text{ac}}$.

Coupled environment-cell model. Representations of *Geobacter* metabolism were coupled to simulations of a dynamic environment through incorporation into a reactive transport model. The two models were connected such that the reactive transport model was used to evaluate the transport of substrate and

Downloaded from http://aem.asm.org/ on July 24, 2020 at ORTA DOGU TEKNIK UNIVERSITESI

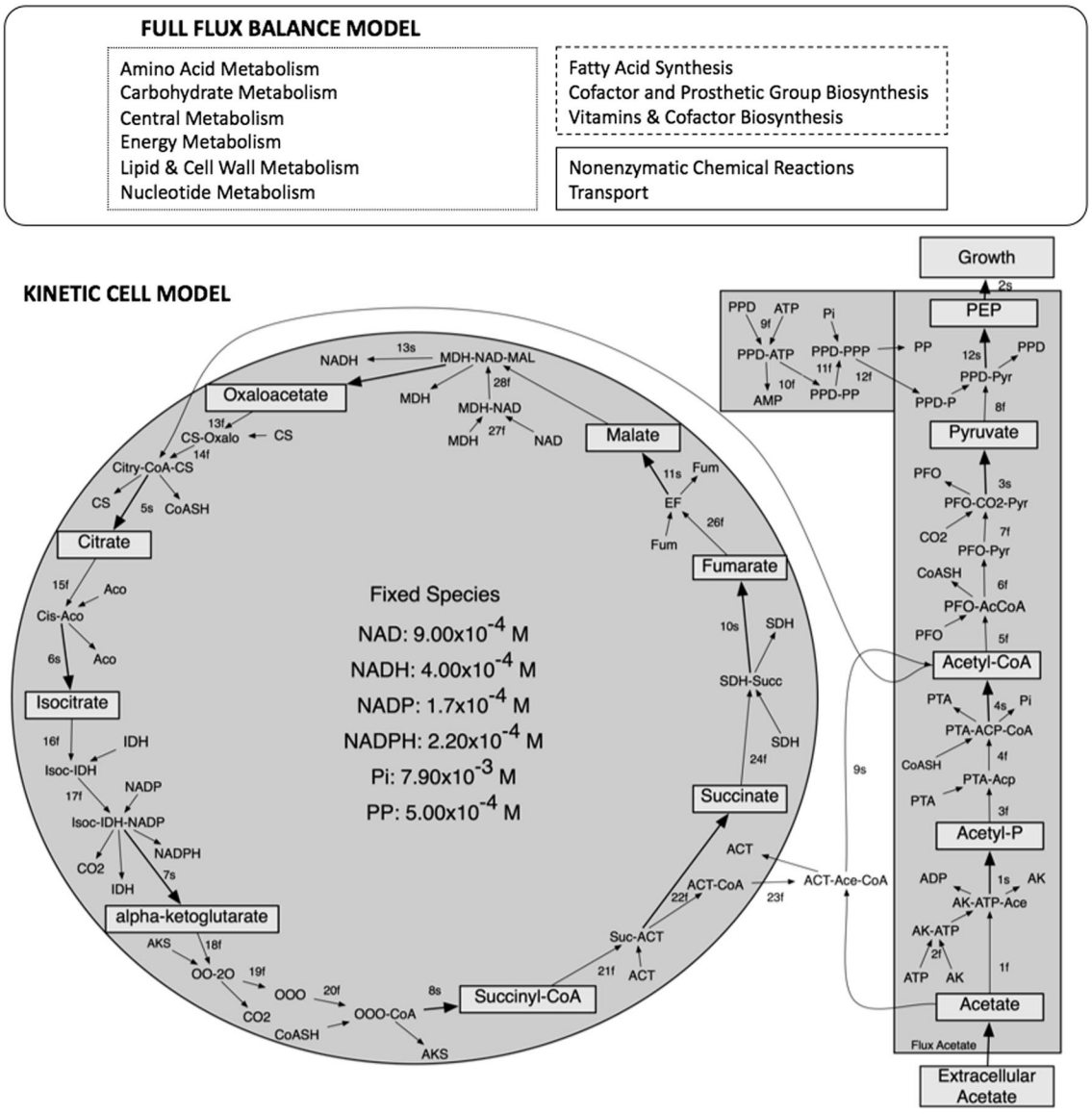


FIG. 1. Structure of the kinetic cell model and FB models. The kinetic model focuses on the fate of acetate in the metabolism of *Geobacter sulfurreducens* through incorporation into biomass from gluconeogenesis or energy production from the TCA cycle. All reactions are assumed to be intrinsically reversible, and the rates are computed using the parameter values listed (for data sources, see the Appendix). The FB model is described in a study by Mahadevan et al. (26) and encompasses some 500 reactions and species.

biomass while the cell model provided the cell-specific reaction rates under the environmental conditions at a given time and location. These cell-specific rates were then used to compute the reaction rates in the macroscopic reactive transport model. For dissolved constituents, the governing equation is

$$\phi\frac{\partial C}{\partial t} = \nabla\cdot(D^*\nabla C) - \nabla\cdot(\phi v C) + \phi\Sigma R \tag{7}$$

where ϕ is porosity, t is time, C is concentration, v is pore water velocity, D^* is the dispersion tensor implemented with dependence on v as described by Scheidegger (36), and ΣR is the net reaction rate. Flow velocities were computed from an imposed pressure gradient using a Darcy model (40).

In our implementation, the cell model was driven by the availability of acetate as the substrate, whose spatiotemporal dynamics proceeded via

$$\frac{\partial C_{ac}}{\partial t} = T_{ac} - R_{ac}^{cell} C_{BM} + R_{ferm} \tag{8}$$

$$\frac{\partial C_{BM}}{\partial t} = T_{BM} + g_{eff} R_{ac}^{cell} C_{BM} \tag{9}$$

where T_{ac} and T_{BM} denote the transport of acetate (C_{ac}) and biomass (C_{BM}), respectively, due to convection and dispersion, g_{eff} is the growth efficiency, R_{ac}^{cell} is the rate of acetate uptake, and R_{ferm} is a source of acetate from the breakdown of high-molecular-weight organics. The model was solved numerically using sequential noniterative operator splitting. In each time step, Δt, first the pressure and flow field were determined, which were then used to calculate the net transport for each of the chemical species. Subsequently, concentration changes due to reactions were evaluated by solving a set of coupled ordinary differential equations at each node. Reaction parameters that depend on the cell model (i.e., g_{eff}, R_{ac}^{cell}) were computed for a given environmental condition and cell state, reflected by the intracellular concentrations, and were assumed constant over a time step. Cell death was considered through negative growth efficiencies, which were obtained when the ATP produced did not completely account for cell maintenance demands and

Downloaded from http://aem.asm.org/ on July 24, 2020 at ORTA DOGU TEKNIK UNIVERSITESI

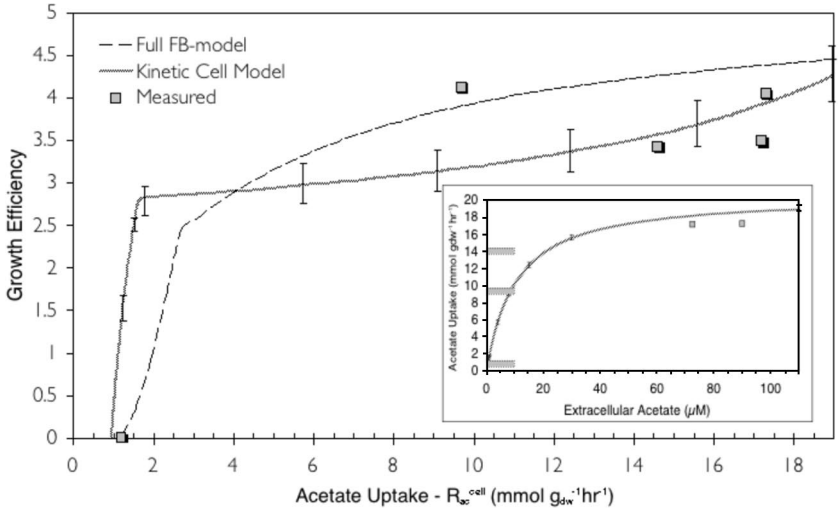


FIG. 2. Growth efficiency in $g_{dw}\ mol_{acetate}^{-1}$ at a given acetate uptake rate (R_{ac}^{cell}) for the cell model, FB model, and measured chemostat data (12). Error bars for the kinetic cell model represent the 25% and 75% quartile ranges, as determined in the sensitivity analysis (see the text). Inset: Acetate uptake flux at a given extracellular acetate concentration computed with the kinetic model along with measured data (chemostat data depicted with filled rectangles indicate measured acetate concentrations below the detection limit of 10 μM).

the existing pool of ATP was insufficient to meet the cellular energy requirements. In that case, the use of biomass resources was considered to meet ATP demands ($a \cdot R_g$; see equation 3).

RESULTS AND DISCUSSION

Model comparison and validation. Experimentally determined growth efficiencies under acetate-limiting conditions are on the order of 4 $g_{dw}\ mol_{acetate}^{-1}$ at uptake fluxes of >10 mmol acetate $g_{dw}^{-1}\ h^{-1}$, and they decrease to 0 at 0.91 mmol $g_{dw}^{-1}\ h^{-1}$ (12). Under replete substrate conditions, growth efficiencies were similar in the FB model and the kinetic description, yielding results consistent with data at high acetate uptake rates (Fig. 2). The fluxes are consistent with those of ^{13}C tracer experiments observed in the isotopic data of Tang et al. (43), which showed that the TCA cycle encompassed ~90% of the acetate uptake flux, with an additional ~8% of acetate flowing through the TCA cycle being used for amino acid and lipid production, and the remainder of the acetate uptake flux passed through the pentose-phosphate pathway and gluconeogenesis. Along with the FB model, the kinetic model predicted that for lower acetate uptake rates, acetate is channeled preferentially into the TCA cycle, leading to low growth efficiency. Both the kinetic and the FB models showed nearly identical responses of the TCA cycle to acetate uptake, with a nearly linear increase in the TCA cycle with increasing acetate uptake rates (not shown). Both models reproduced the general trend in growth efficiencies seen in the literature as a function of the acetate uptake rate (Fig. 2), reflecting that at elevated uptake rates, the portion of acetate following the growth reaction pathway increased relative to that for the TCA cycle.

In contrast to the FB approach, which does not contain information on intracellular concentrations or provide an explicit connection to extracellular substrate levels, the kinetic model mechanistically relates intracellular process rates to extracellular concentrations of acetate. Its results can therefore be parameterized as a function of acetate availability and provide an explicit link between intracellular processes and extracellular conditions. At low extracellular acetate concentrations (μM), acetate uptake responds strongly to changes in substrate availability (Fig. 2, inset). Assuming Michaelis-Menten kinetics, $R_{ac}^{cell} = v_{max}\dfrac{C_{ac}}{K_m(\text{acetate}) + C_{ac}}$, and using steady-state cell model results, one obtained $v_{max} = (19.54 \pm 0.04)\ mmol_{ac}\ g_{dw}^{-1}\ h^{-1}$ and $K_m(\text{acetate}) = (10.24 \pm 0.11) \times 10^{-6}$ mol $liter^{-1}$, consistent with half-saturation constants and maximum uptake rates derived from experimental data (12).

The kinetic model also provides estimates of intracellular metabolite concentrations, which can be used as diagnostics to experimentally assess its validity and limitations. Under steady-state conditions, the cell model predicted malate concentrations in the mM range, consistent with predictions of high malate concentrations based on the thermodynamics of the malate dehydrogenase reaction (5). Several other substances, including oxaloacetate, citrate, isocitrate, and succinate were predicted—depending on growth conditions—to be present in the micro- to millimolar range and to increase by a factor of 10 to 30 between no-growth and maximum-growth conditions. Succinyl coenzyme A (CoA) concentration was predicted to be relatively constant, while significant variations under changing growth conditions were computed for pyruvate and α-ketoglutarate, with lower concentrations at higher growth rates.

Model sensitivity. The sensitivity analysis based on ≥1,000 realizations for a given extracellular acetate concentration, which was sufficient to establish the probability distribution of the model response, allowed the identification of the reactions affecting growth efficiency most strongly (Fig. 3). The extent to which a parameter affected growth efficiency varies with the acetate uptake rate. For example, at low acetate uptake rates, growth efficiency was most sensitive toward parameters describing the acetate-CoA transferase (ACT; EC 2.8.3.8) reaction. In general, however, growth efficiency, over the range of acetate uptake rates, was most sensitive to cell model param-

Downloaded from http://aem.asm.org/ on July 24, 2020 at ORTA DOGU TEKNIK UNIVERSITESI

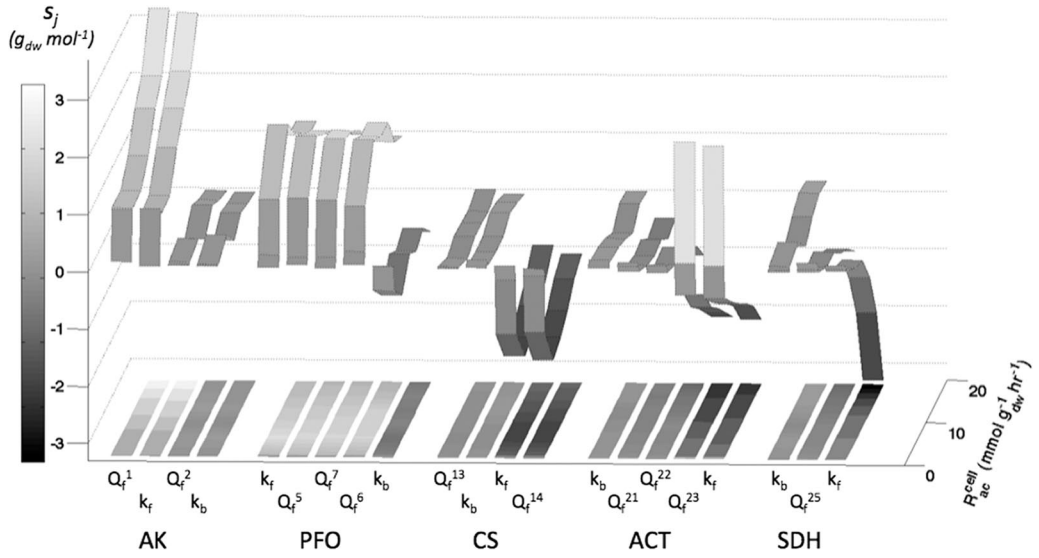


FIG. 3. Sensitivity, s_j, of growth efficiencies to perturbations in the cell model parameters as a function of acetate uptake rates (equation 2). Labels AK, CS, ACT, SDH and PFO along the bottom of the figure denote the reactions promoted by the respective enzymes (see Fig. 1). k_b, k_f, and Q values denote the model parameters. Large absolute values of s_j indicate a strong impact of a model parameter on resulting growth efficiencies (see the text for details).

eters associated with the activation of acetate to acetyl-P catalyzed by AK (Fig. 3), a reaction essential to the use of acetate in biomass production, as all acetate incorporated into cell biomass must go through this reaction (26). Increasing the forward rate constant k_f—corresponding to an increase in enzyme concentration (E_T), maximum enzyme activity (v_{max}), or higher substrate affinity (lower K_m)—involved in the reaction catalyzed by citrate synthase (CS; EC 2.3.3.1) decreased growth efficiencies as more acetyl-CoA is shifted to the TCA cycle. For the same reason, increasing the parameters associated with the reaction catalyzed by succinate dehydrogenase (SDH; EC 1.3.99.1) resulted in a decrease in growth efficiency, and increasing parameters associated with pyruvate ferredoxin oxidoreductase (PFO; EC 1.2.7.1), a reaction involved in growth, resulted in an increase in growth efficiency. The variation in growth efficiency due to small—on the order of 5%—variations in forward and backward reaction rate constants can largely (>95%) be explained by the linear model (equation 2). Uncertainties in E_T, v_{max}, and K_m, however, tend to result in larger uncertainties in growth efficiencies due to error propagation, but the same reactions are found to have the most decisive impact (not shown).

Environmental setting. Reactive transport models often do not—or only in a simplistic manner—reflect microbial population dynamics (22). To assess the importance of dynamically resolving cellular metabolism, where the rates depend on both extracellular and intracellular concentrations, reactive transport simulations with the full kinetic cell model (model I) were compared with three parameterized versions. The first used a lookup table established from steady-state runs of the kinetic cell model so that cell-specific rates were expressed as a function of extracellular conditions, but it did not take into account intracellular dynamics and assumed that intracellular metabolite concentrations have reached a steady state. Because computed intracellular metabolite concentrations (at least at the level resolved in the kinetic cell model) adjusted to changes in substrate availability over timescales in seconds, consistent with observed intracellular dynamics in bacteria (e.g., see reference 35), the results from the steady-state cell model were virtually indistinguishable from those of model I and are hence not shown separately. The second implementation (model II) simplified the approach further, to a level typically used in reactive transport models, assuming that cell-specific growth efficiency (g_{eff}; equations 8 and 9) is constant and that acetate uptake (R_{ac}^{cell}; equations 8 and 9) can be expressed by Monod kinetics, with K_m(acetate) = 10.24 μM and v_{max} = 19.54 mmol g_{dw}^{-1} h^{-1}, as derived above. Finally, a third approximation employed both a constant growth efficiency and a constant acetate uptake rate as long as acetate was present (model III), with a cell-specific acetate uptake rate of 9×10^{-3} $mol_{acetate}$ g_{dw}^{-1} h^{-1} and a growth efficiency of 3.3 g_{dw} $mol_{acetate}^{-1}$ (12).

In order to quantify the impact of microbial dynamics and the substrate dependence of growth efficiencies under environmental conditions, simulations were performed in a domain that was 10 cm long and 6 cm high. The porous medium consisted of permeable sand ($k = 10^{-11}$ m^2) into which a less permeable section was embedded ($k = 10^{-13}$ m^2) as depicted in Fig. 4. No-flow conditions were set at the upper and lower domain boundaries, and a positive pressure gradient was imposed across the horizontal x-direction. The inflowing fluid was set to contain 0.76 μM acetate and 0.03 g_{dw} m^{-3} biomass. After a period of constant input that allowed the establishment of a steady substrate and biomass distribution, the concentrations in the inflowing fluid were ramped up over a duration of 1 h to an inflow concentration of 1 mM acetate and 0.3 g_{dw} m^{-3} biomass, reflecting a plume of dissolved organic carbon (16), and were held constant at high levels thereafter.

Steady-state biomass and acetate distributions under pristine conditions showed distinct differences between the various models. For all representations, relatively low, uniform bio-

Downloaded from http://aem.asm.org/ on July 24, 2020 at ORTA DOGU TEKNIK UNIVERSITESI

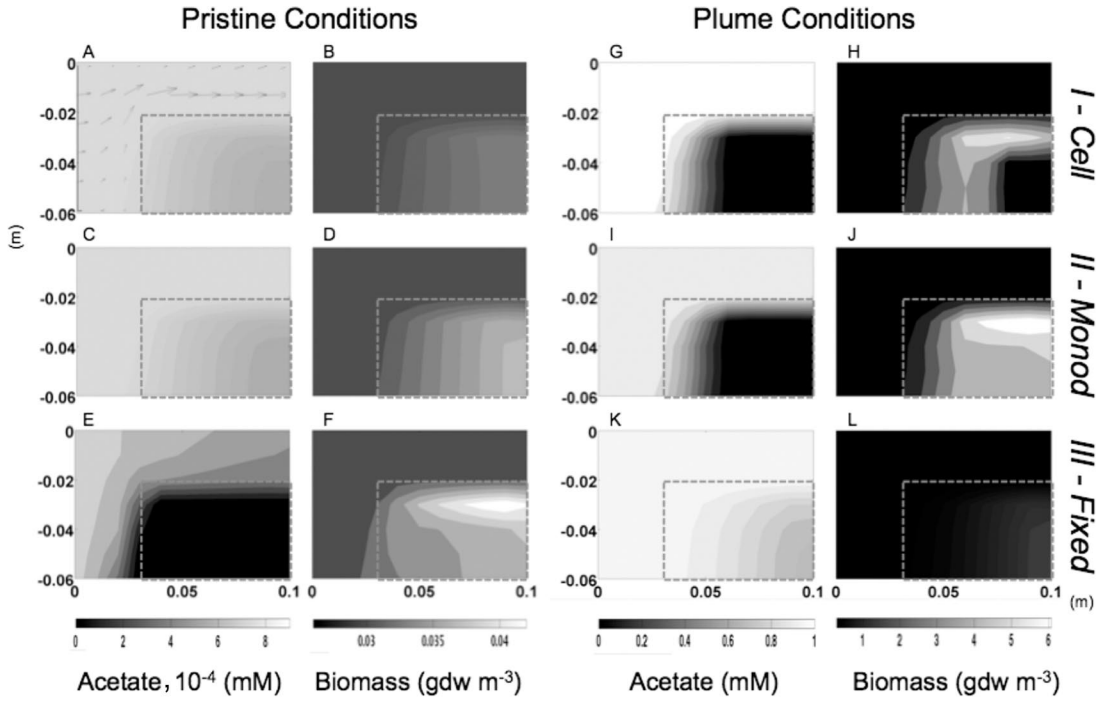


FIG. 4. Results of reactive simulations utilizing different representations of bacterial growth and acetate uptake. Steady-state acetate and biomass distributions under low (panels A to F) and high (panels G to L) input conditions for the dynamic cell model (panels A, B, G, and H), the Monod parameterization (panels C, D, I, and J), and simulations with fixed growth efficiency and acetate uptake rate (panels E, F, K, and L). The low-permeability zone is indicated by the boxes with dashed-line borders, and the arrows in panel A indicate the direction and magnitude of flow.

mass distributions were observed (Fig. 4B, D, and F). However, the fixed uptake and growth efficiency formulation (model III) predicted spatially various acetate concentrations, with lower levels in the low-permeability zone (Fig. 4E). This drawdown was caused by the slightly elevated biomass concentrations in that region (Fig. 4F), because this approximation contains no feedback between substrate level and the allocation of acetate to growth versus catabolism that would lower uptake rates at low substrate availability. Results from model II (Fig. 4A and C) closely matched those from model I (Fig. 4B and D), despite that at low acetate concentrations, the Monod approximation and cell model differed in their growth efficiency. This is because at low acetate levels, cell-specific acetate uptake rates are low. In addition, the Monod model does not take into account cell death, which, when included, became important for regulating biomass levels in the pristine setting at cell death rates on the order of 10% of the growth rate (not shown).

Steady high substrate input stimulated microbial growth, reflected in the elevated biomass levels in both high- and low-permeability regions (Fig. 4H, J, and L). A clear distinction was visible between the results obtained with the dynamic cell model and the Monod approximations compared to the fixed growth efficiency description. The latter predicted biomass levels ranging from 0.3 to 1.2 g_{dw} m^{-3} in the low-permeability zone (Fig. 4L), while the kinetic models suggested a region of higher biomass in the low-permeability zone adjacent to the more-permeable one (Fig. 4H and J). In the models that represented the cell in more detail, the maximum growth efficiencies exceeded the constant average value in the "fixed" model, leading to a buildup of biomass and the depletion of acetate in the low-permeability zone. The Monod parameterized model suggested acetate levels that are similar to those for the cell model (Fig. 4G and I). The cell model predicted the depletion of biomass in those low-permeability regions that exhibited low acetate concentrations (Fig. 4H). This pattern was less pronounced in the Monod model, which as a result of the missing feedback of substrate availability on growth efficiencies showed elevated biomass levels even where acetate levels approached zero (Fig. 4I and J).

Conclusion. The kinetic representation of *Geobacter sulfurreducens* central metabolism, encompassing its TCA cycle and the use of pyruvate in gluconeogenesis, successfully reproduces measured growth efficiencies, with iron as electron acceptor over a wide range of extracellular acetate concentrations. Despite its limited scope, it predicts process rates that are in good agreement with results from a comprehensive FB model (26), as it includes feedback between metabolite levels and transformation rates which can accurately regulate the response over a range of substrate conditions.

The two main differences between these two modeling approaches are the extents of the network considered and the fact that the kinetic description provides explicit estimates of intracellular metabolite concentrations. The more comprehensive description inherent in FB models—possible because they do not require extensive parameterization—is an advantage as, intrinsically, it extends the range of applicability well beyond the acetate-limited environmental settings discussed here.

Downloaded from http://aem.asm.org/ on July 24, 2020 at ORTA DOGU TEKNIK UNIVERSITESI

However, the computation of metabolite levels in the kinetic approach allows for a mechanistic process description linking intracellular conditions to environmental conditions. In contrast, the FB approach requires a priori knowledge of uptake fluxes, which may restrict its use to settings at which they are constrained by experimental data.

While comparison of the fully coupled reactive transport model with the Monod type simulations shows that it is possible to approximate microbial distribution patterns without the explicit incorporation of cell models into reactive transport simulations, the parameterization has to reflect the response of intracellular processes. Process-level descriptions of microbial metabolism give rise to emerging properties, such as growth efficiencies, that are critical in the incorporation of microbial dynamics in reactive transport models. Hence, models aiming at describing in situ microbial functioning and at accounting for environmental feedbacks can benefit substantially from reflecting the growing knowledge on cellular metabolism, which in turn will bolster the predictive power necessary for their broad application.

APPENDIX

To derive estimates of rate and equilibrium constants required in the model, literature data were mined and converted into the format required for the cell model. Whenever available, enzyme turnover numbers were used, as they represent a measurement of kQ_s (s^{-1}). However, this parameter was not often available, so kQ_s values were derived from reported *Geobacter* enzymatic specific activities. Specific activity from pure enzyme extract was converted into a forward rate constant, kQ_s (s^{-1}), by

$$kQ_s = \mathrm{SA}_{\mathrm{pure}} \cdot \mathrm{MW} \tag{A1}$$

where $\mathrm{SA}_{\mathrm{pure}}$ ($\mathrm{mol}^{-1}\ \mathrm{g}_{\mathrm{enzyme}}{}^{-1}$) is the specific activity measured from the pure enzyme extract and MW is the molecular weight of an enzyme subunit (g mol^{-1}). Specific activity measured from the crude enzyme fraction was converted into an in situ v_{max} (mol $\mathrm{liter}^{-1}\ \mathrm{s}^{-1}$) value, as described by Albe et al. (1) by using

$$v_{\mathrm{max}} = \mathrm{SA}_{\mathrm{crude}} \cdot f_{\mathrm{prot}} \cdot \frac{g_{\mathrm{bm}}}{V_{\mathrm{cell}}} \tag{A2}$$

where $\mathrm{SA}_{\mathrm{crude}}$ (mol $\mathrm{s}^{-1}\ \mathrm{g}_{\mathrm{protein}}{}^{-1}$) is measured from the crude enzyme fraction, f_{prot} is the fraction of cell biomass that is protein, determined to be 0.46 (26), g_{bm} is grams of dry weight of biomass per cell, determined to be 40 fg, and V_{cell} is the cell volume, determined to be 4.91×10^{-16} liters, calculated based on *G. sulfurreducens* cell size (37) assuming a cylindrical shape. This v_{max} value was converted to kQ_s for implementation into Karyote (31) according to

$$kQ_s = \frac{v_{\mathrm{max}}}{E_T} \tag{A3}$$

where E_T is the total enzyme concentration. The parameter, kQ_s, was converted into k and Q_s values for implementation of the slow reaction dynamics into the cell model. Values of Q_s were calculated according to

$$Q_s = \frac{Q_T}{\Pi Q_{fi}} \tag{A4}$$

where Q_T is the equilibrium constant for the overall net reaction based on thermodynamic data, obtained from a study by Goldberg et al. (15), and Q_{fi} is the equilibrium constant for the ith fast reaction in each mechanism. Equilibrium constants for the fast reactions—and slow reactions when no thermodynamic data were available to estimate Q_T—were determined from

$$Q_i = \prod_k C_k^{\nu_{ik}} \tag{A5}$$

where C_k represents the equilibrium concentration of species k in reaction i in the enzyme mechanisms below, and ν_{ik} is its stoichiometric coefficient (positive for products, negative for reactants).

Concentrations of enzyme substrate complexes used in equation A5 are not measured directly and were calculated according to each enzyme's mechanism, which is separated into several fast components and one slow component (32):

isomerization reaction $E + S \overset{\text{fast}}{\longleftrightarrow} ES \overset{\text{slow}}{\longleftrightarrow} E + P$

bi-bi ordered reaction $E + S_1 \overset{\text{fast}}{\longleftrightarrow} (ES)_1$

$(ES)_1 + S_2 \overset{\text{fast}}{\longleftrightarrow} (ES)_2 \overset{\text{slow}}{\longleftrightarrow} E + P_1 + P_2$

ping-pong reaction $E + S_1 \overset{\text{fast}}{\longleftrightarrow} (ES)_1 \overset{\text{fast}}{\longleftrightarrow} (ES)_2 + P_1$

$(ES)_2 + S_2 \overset{\text{fast}}{\longleftrightarrow} (ES)_3 \overset{\text{slow}}{\longleftrightarrow} P_2 + E$

tri-ping-pong reaction $E + S_1 \overset{\text{fast}}{\longleftrightarrow} (ES)_1 \overset{\text{fast}}{\longleftrightarrow} (ES)_2 + P_1$

$(ES)_2 + S_2 \overset{\text{fast}}{\longleftrightarrow} (ES)_3 \overset{\text{fast}}{\longleftrightarrow} P_2 + (ES)_4$

$(ES)_4 + S_3 \overset{\text{fast}}{\longleftrightarrow} (ES)_5 \overset{\text{slow}}{\longleftrightarrow} P_3 + E.$

The enzyme substrate concentrations in the slow reactions were calculated following Purich and Allison (32):

isomerization reaction

$$ES = \frac{E_T \cdot [S]}{Km_1 + [S]} \tag{A6}$$

ordered bi-bi reaction

$$(ES)_2 = \frac{E_T \cdot [S_1] \cdot [S_2]}{Km_1 \cdot Km_2 + [S_1] \cdot Km_2 + [S_1] \cdot [S_2]} \tag{A7}$$

ping-pong reaction

$$(ES)_3 = \frac{E_T \cdot [S_1] \cdot [S_2]}{Km_2 \cdot [S_1] + [S_2] \cdot Km_1 + [S_1] \cdot [S_2]} \tag{A8}$$

Downloaded from http://aem.asm.org/ on July 24, 2020 at ORTA DOGU TEKNIK UNIVERSITESI

TABLE A1. Values used for the parameterization of the reaction network[f]

Enzyme[a]	Enzyme total (M)	Sp act[b]	*Km* value (M)[c]	Q_T[d]	*k*	Reaction index[e] and *Q* value
ACO	1×10^{-6} (41)	240 (18)	$Km_{citrate} = 1 \times 10^{-2}$ (9)	6.80×10^{-2}	2.20e5 M^{-1} s^{-1}	15f, 1.00e2 M^{-1} 6s, 6.80e−2 M
ACT	1×10^{-6} (41)	900 (18)	$Km_{succ\text{-}coa} = 1.5 \times 10^{-4}$ (19) $Km_{acetate} = 5 \times 10^{-4}$ (19)	N/A*	3.25e5 M^{-1} s^{-1}	21f, 6.67e3 M^{-1} 22f, 1.96e−3 M^{1} 23f, 2.00e3 M^{-1} 9s, 1.73e−1 M
AK	2.26×10^{-5} (1)	22.8 (13)	$Km_{ATP} = 7 \times 10^{-5}$ (17) $Km_{acetate} = 3 \times 10^{-1}$ (21)	8.70×10^{-3}	7.69e8 M^{-2} s^{-1}	1f, 7.69 M^{-1} 1s, 7.92e−8 M^{2} 2f, 1.43e4 M^{-1}
CS	1.73×10^{-4} (7)	8.3 (7)	$Km_{oxaloacetate} = 4.3 \times 10^{-6}$ (7) $Km_{acetyl\text{-}CoA} = 1.41 \times 10^{-5}$ (7)	N/A*	3.94e6 M^{-2} s^{-1}	13f, 2.33e5 M^{-1} 14f, 7.09e4 M^{-1} 5s, 2.11e−4 M^{2}
FUM	1×10^{-6} (41)	320.9 (13)	$Km_{fumarate} = 2.3 \times 10^{-5}$ (18)	4.43	1.97e6 M^{-1} s^{-1}	26f, 4.35e4 M^{-1} 11s, 1.02e−2 M
IDH	4.74×10^{-5} (1)	40.8 (13)	$Km_{isocitrate} = 8 \times 10^{-4}$ (19) $Km_{NADP} = 1.7 \times 10^{-5}$ (25)	9.3×10^{-1}	4.25e7 M^{-3} s^{-1}	16f, 1.25e3 M^{-1} 17f, 5.88e4 M^{-1} 7s, 1.26e−6 M^{3}
MDH	1×10^{-6} (41)	471.5 (13)	$Km_{malate} = 5 \times 10^{-3}$* (7) $Km_{NAD} = 9 \times 10^{-4}$* (35)	1.2×10^{-5}	5.45e12 M^{-2} s^{-1}	27f, 1.11e3 M^{-1} 28f, 2.00e2 M^{-1} 13s, 5.40e−9 M^{2}
AKS	1×10^{-6} (41)	52.2 (13)	$Km_{akg} = 2 \times 10^{-3}$ (19) $Km_{CoA} = 4 \times 10^{-5}$ (19)	N/A*	3.71e5 M^{1} s^{-1}	18f, 5.00e2 M^{-1} 19f, 6.35e−4 M 20f, 2.50e4 M^{-1} 8s, 8.78e−3 M^{-1}
PFO	1×10^{-6} (41)	120 (19)	$Km_{acetyl\text{-}CoA} = 7 \times 10^{-5}$ (19)	N/A*	5.77e6 M^{-1} s^{-1}	5f, 1.43e4 M^{-1} 6f, 5.61e−4 M 7f, 8.33e2 M^{-1} 3s, 1.30e−3 M
PPD	1×10^{-6} (41)	5,900 (51)	$Km_{ATP} = 2 \times 10^{-4}$ (51) $Km_{AMP} = 6 \times 10^{-6}$ (51) $Km_{Pi} = 8.3 \times 10^{-4}$ (51) $Km_{pyruvate} = 2.7 \times 10^{-5}$ (51)	1.45×10^{-3}	3.78e6 M^{-1} s^{-1}	8f, 3.70e4 M^{-1} 12s, 1.43e−4 M 9f, 5.00e3 M^{-1} 10f, 6.00e−6 M 11f, 1.20e3 M^{-1} 12f, 7.56e−4 M
PTA	1×10^{-6} (1)	48.0 (13)	$Km_{acetyl\text{-}P} = 3 \times 10^{-4}$* (38) $Km_{CoA} = 9.36 \times 10^{-5}$* (14)	1.47×10^{2}	7.26e6 M^{-2} s^{-1}	3f, 3.33e3 M^{-1} 4f, 1.07e4 M^{-1} 4s, 4.13e−4 M^{2}
SDH	8.93×10^{-5} (1)	10.2 (13)	$Km_{succinate} = 5 \times 10^{-4}$ (19)	N/A*	7.94e3 M^{-2} s^{-1}	24f, 2.00e3 M^{-1} 10s, 8.98e−4 M^{2}

[a] Aconitase (ACO; EC 4.2.1.3), fumarase (FUM; EC 4.2.1.2), and SDH (EC 1.3.99.1) employed an isomerization mechanism; acetate kinase (AK; EC 2.7.2.1), citrate synthase (CS; EC 2.3.3.1), isocitrate dehydrogenase (IDH; EC 1.1.1.42), malate dehydrogenase (MDH; EC 1.1.1.37), and phosphate acetyl transferase (PTA; EC 2.3.1.8) employed an ordered bi-bi mechanism; ACT (EC 2.8.3.8), α-ketoglutarate synthase (AKS; EC 1.2.7.3), and PFO (EC 1.2.7.1) employed a ping-pong mechanism; and pyruvate phosphate dikinase (PPD; EC 2.7.9.1) employed a tri-ping-pong mechanism.

[b] Specific activities for ACO, ACT, AK, FUM, IDH, MDH, AKS, PFO, PTA, and SDH were measured from the crude enzyme fraction, and that for PPD was measured from the pure enzyme fraction (nmol min^{-1} $mg_{protein}{}^{-1}$). Specific activity for CS was derived from enzyme turnover numbers, k_{cat} (s^{-1}).

[c] akg, α-ketoglutarate; succ-coa, succinyl-CoA.

[d] Q_T denotes the equilibrium constant for the overall net reaction based on thermodynamic data, obtained from reference 15. N/A* indicates that the equilibrium constant for the slow reaction is derived from typical species concentrations.

[e] Fast reactions are denoted by "f," slow reactions by "s." The numbers preceding the letters "f" and "s" refer to the reactions labeled in Fig. 1.

[f] Numbers in parentheses indicate the reference used. Data denoted with an asterisk (*) are estimates that are based on the following typical substrate concentrations (units, M): oxaloacetate, 1×10^{-7} (5); malate, 5×10^{-3} (5); acetyl-CoA, 3.5×10^{-4} (1); PEP, 9.1×10^{-5} (1); fumarate, 3×10^{-5} (1); citrate, 1.3×10^{-2} (1); α-ketoglutarate, 4.76×10^{-4} (1); ATP, 2.64×10^{-3} (1); ADP, 8.23×10^{-4} (1); AMP, 1.51×10^{-4} (1); pyruvate, 3.9×10^{-4} (1); CoA, 9.36×10^{-5} (11); succinate, 1.67×10^{-3} (47); isocitrate, 2.9×10^{-5} (47); acetyl-P, 3×10^{-4} (28); succinyl-CoA, 2.59×10^{-5} (19); acetate, 5×10^{-4} (14). These values were also used to estimate Q_f (equation A5).

tri-ping-pong reaction

$$(ES)_5 = \frac{E_T \cdot [S_1] \cdot [S_2] \cdot [S_3]}{Km_1 \cdot [S_2] \cdot [S_3] + Km_2 \cdot [S_1] \cdot [S_3] + Km_3 \cdot [S_1] \cdot [S_2] + [S_1] \cdot [S_2] \cdot [S_3]} \quad \text{(A9)}$$

where $[S_1]$, $[S_2]$, and $[S_3]$ are the typical cell concentrations of the first, second, and third substrates to bind with the enzyme, respectively, and Km_1, Km_2, and Km_3 are the half-saturation constants for substrates 1, 2, and 3, respectively. The enzyme substrate complexes involved in the fast reactions were then calculated according to equations A10 to A16, as follows:

for enzymes that employ an ordered bi-bi mechanism,

$$[(ES)_1] = \frac{Km_2 \cdot [(ES)_2]}{[S_2]} \quad \text{(A10)}$$

for enzymes that employ a ping-pong mechanism,

$$[(ES)_2] = \frac{Km_2 \cdot [(ES)_3]}{[S_2]} \quad \text{(A11)}$$

Downloaded from http://aem.asm.org/ on July 24, 2020 at ORTA DOGU TEKNIK UNIVERSITESI

$$[(ES)_1] = \frac{([E_T] - [(ES)_2] - [(ES)_3]) \cdot [S_1]}{[S_1] + Km_1} \quad \text{(A12)}$$

for a tri-ping-pong mechanism,

$$[(ES)_1] = \frac{[(ES)_3] \cdot Km_2 \cdot [P_1]}{[S_2] + Km_{p1}} \quad \text{(A13)}$$

$$[(ES)_2] = \frac{Km_2 \cdot [(ES)_3]}{[S_2]} \quad \text{(A14)}$$

$$[(ES)_3] = \frac{[E_T] - [(ES)_5] - [(ES)_4]}{1 + \frac{Km_2}{[S_2]} + \frac{Km_2 \cdot [P_1]}{[S_2] \cdot Km_{p1}} + \frac{Km_2 \cdot [P_1] \cdot Km_1}{[S_2] \cdot Km_{p1} \cdot [S_1]}} \quad \text{(A15)}$$

$$[(ES)_4] = \frac{Km_3 \cdot [(ES)_5]}{[S_3]} \quad \text{(A16)}$$

where ES represents the enzyme substrate complexes, Km_i the half-saturation constant of the ith substrate, Km_{p1} the half-saturation constant for the ith product released, S_j the jth substrate in the enzymatic reaction, and P_j the jth product released. As the determination of Q_s values is subject to considerable uncertainties and does not take into account chemical speciation in the highly complex intracellular fluid, all values were adjusted by a factor of 100, which led to TCA cycle rates consistent with observations.

The values used for the parameterization of the reaction network are shown in Table A1.

ACKNOWLEDGMENTS

This work was supported by the Department of Energy Office of Science grant DE-FG02-05ER25676.

We thank two anonymous reviewers, whose comments significantly improved the manuscript.

REFERENCES

1. **Albe, K. R., M. H. Butler, and B. E. Wright.** 1990. Cellular concentrations of enzymes and their substrates. J. Theor. Biol. **143:**163–195.
2. **Bakker, B. M., P. A. M. Michels, F. R. Opperdoes, and H. V. Westerhoff.** 1997. Glycolysis in bloodstream from Trypanosoma brucei can be understood in terms of the kinetics of the glycolytic enzymes. J. Biol. Chem. **272:**3207–3215.
3. **Bear, J.** 1972. Dynamics of fluids in porous media. American Elsevier Publishing Company, Inc., New York, NY.
4. **Behrends, T., and P. Van Cappellen.** 2005. Competition between enzymatic and abiotic reduction of uranium(VI) under iron reducing conditions. Chem. Geol. **220:**315–327.
5. **Bond, D. R., T. Mester, C. L. Nesbo, A. V. Izquierdo-Lopez, F. L. Collart, and D. R. Lovley.** 2005. Characterization of citrate synthase from *Geobacter sulfurreducens* and evidence for a family of citrate synthases similar to those of eukaryotes throughout the *Geobacteraceae*. Appl. Environ. Microbiol. **71:**3858–3865.
6. **Bradley, P. M., and F. H. Chapelle.** 1996. Anaerobic mineralization of vinyl chloride in Fe(II)-reducing aquifer sediments. Environ. Sci. Technol. **30:** 2084–2086.
7. **Brun, A., P. Engesgaard, T. H. Christensen, and D. Rosbjerg.** 2002. Modeling of transport and biogeochemical processes in pollution plumes: Vejen landfill, Denmark. J. Hydrol. **256:**228–247.
8. **Caccavo, F. J., D. Lonergan, D. R. Lovley, M. Davis, J. F. Stolz, and M. J. McInerney.** 1994. *Geobacter sulfurreducens* sp. nov., a hydrogen- and acetate-oxidizing dissimilatory metal-reducing microorganism. Appl. Environ. Microbiol. **60:**3752–3759.
9. **Canfield, D. E., E. Kristensen, and B. Thamdrup.** 2005. Aquatic geomicrobiology. Elsevier Academic Press, New York, NY.
10. **Champine, J. E., and S. Goodwin.** 1991. Acetate catabolism in the dissimilatory iron-reducing isolate GS-15. J. Bacteriol. **173:**2704–2706.
11. **Chohnan, S., T. Nagata, and Y. Midorikawa.** 1994. Purification and characterization of a novel bifunctional enzyme, cyclic-ribonucleotide phosphomutase-5′-phosphodiesterase, from Aspergillus niger. Biosci. Biotechnol. Biochem. **58:**250–255.
12. **Esteve-Núñez, A., M. Rothermich, M. Sharma, and D. R. Lovley.** 2005. Growth of Geobacter sulfurreducens under nutrient-limiting conditions in continuous culture. Environ. Microbiol. **7:**641–648.
13. **Forster, J., I. Famili, P. Fu, B. O. Palsson, and J. Nielsen.** 2003. Genome-scale reconstruction of the Saccharomyces cerevisiae metabolic network. Genome Res. **13:**244–253.
14. **Gebhardt, N. A., R. K. Thauer, D. Linder, P. M. Kaulfers, and N. Pfennig.** 1985. Mechanism of acetate oxidation to CO_2 with elemental sulfur in Desulfuromonas acetoxidans. Arch. Microbiol. **141:**392–398.
15. **Goldberg, R. N., Y. B. Tewari, and T. N. Bhat.** 2004. Thermodynamics of enzyme-catalyzed reactions—a database for quantitative biochemistry. Bioinformatics **20:**2874–2877.
16. **Gunten, U. V., and J. Zobrist.** 1993. Biogeochemical changes in groundwater-infiltration systems: column studies. Geochim. Cosmochim. Acta **57:**3895–3906.
17. **Herbel, M., and S. Fendorf.** 2006. Biogeochemical processes controlling the speciation and transport of arsenic within iron coated sands. Chem. Geol. **228:**16–32.
18. **Hunter, K. S., Y. Wang, and P. Van Cappellen.** 1998. Kinetic modeling of microbially-driven redox chemistry in subsurface environments: coupling transport, microbial metabolism and geochemistry. J. Hydrol. **209:**53–58.
19. **Jackowski, S., and C. O. Rock.** 1986. Consequences of reduced intracellular coenzyme—a content in *Escherichia coli*. J. Bacteriol. **166:**866–871.
20. **Jeong, H., B. Tombor, R. Albert, Z. N. Oltavai, and A.-L. Barbasi.** 2000. The large-scale organization of metabolic networks. Nature **407:**651–654.
21. **Leang, C., M. V. Coppi, and D. R. Lovley.** 2003. OmcB, a c-type polyheme cytochrome, involved in Fe(III) reduction in *Geobacter sulfurreducens*. J. Bacteriol. **185:**2096–2103.
22. **Lovley, D. R.** 2003. Cleaning up with genomics: applying molecular biology to bioremediation. Nat. Rev. Microbiol. **1:**35–44.
23. **Lovley, D. R.** 1993. Dissimilatory metal reduction. Annu. Rev. Microbiol. **47:**263–290.
24. **Lovley, D. R., D. E. Holmes, and K. P. Nevin.** 2004. Dissimilatory Fe(III) and Mn(IV) reduction. Adv. Microb. Physiol. **49:**219–286.
25. **Lovley, D. R., E. J. P. Phillips, Y. A. Gorby, and E. R. Landa.** 1991. Microbial reduction of uranium. Nature **350:**413–416.
26. **Mahadevan, R., D. R. Bond, J. E. Butler, A. Esteve-Nunez, M. V. Coppi, B. O. Palsson, C. H. Schulling, and D. R. Lovley.** 2006. Characterization of metabolism in the Fe(III)-reducing organism *Geobacter sulfurreducens* by constraint-based modeling. Appl. Environ. Microbiol. **72:**1558–1568.
27. **Mauclaire, L., O. Pelz, M. Thullner, W. R. Abraham, and J. Zeyer.** 2003. Assimilation of toluene carbon along a bacteria-protist food chain determined by C-13-enrichment of biomarker fatty acids. J. Microbiol. Methods **55:**635–649.
28. **McCleary, W. R., and J. B. Stock.** 1994. Acetyl phosphate and the activation of 2-component response regulators. J. Biol. Chem. **269:**31567–31572.
29. **Methé, B. A., K. E. Nelson, J. A. Eisen, I. T. Paulsen, W. Nelson, J. F. Heidelberg, D. Wu, M. Wu, N. Ward, M. J. Beanan, R. J. Dodson, R. Madupu, L. M. Brinkac, S. C. Daugherty, T. R. DeBoy, A. S. Durkin, M. Gwinn, J. F. Dolonay, S. A. Sullivan, D. H. Haft, J. Selengut, T. M. Davidsen, N. Zafar, O. White, B. Tran, C. Romerio, H. A. Forberger, J. Weidman, H. Khouri, T. V. Feldblyum, T. R. Utterback, S. E. Van Aken, D. R. Lovley, and C. M. Fraser.** 2003. Genome of Geobacter sulfurreducens: metal reduction in subsurface environments. Science **302:**1967–1969.
30. **Navid, A., and P. J. Ortoleva.** 2004. Simulated complex dynamics of glycolysis in the protozoan parasite Trypanosoma brucei. J. Theor. Biol. **228:**449–458.
31. **Ortoleva, P., E. Berry, Y. Brun, J. Fan, M. Fontus, K. Hubbard, K. Jaqaman, L. Jarymowycz, A. Navid, A. Sayyed-Ahmad, Z. Shreif, F. Stanley, K. Tuncay, E. Weitzke, and L.-C. Wu.** 2003. The Karyote physico-chemical genomic, proteomic metabolomic cell modeling system. OMICS **7:**269–283.
32. **Purich, D. L., and R. D. Allison.** 1999. Handbook of biochemical kinetics. Academic Press, San Diego, CA.
33. **Reed, J. L., T. D. Vo, C. H. Schilling, and B. O. Palsson.** 2003. An expanded genome-scale model of Escherichia coli K-12 (iJR904 GSM/GPR). Genome Biol. **4:**R54.
34. **Rockhold, M. L., R. R. Yarwood, and J. S. Selker.** 2004. Coupled microbial and transport processes in soils. Vadose Zone J. **3:**368–383.
35. **Schaefer, U., W. Boos, R. Takors, and D. Weuster-Botz.** 1999. Automated sampling device for monitoring intracellular metabolite dynamics. Anal. Biochem. **270:**88–96.
36. **Scheidegger, A. E.** 1961. General theory of dispersion in porous media. J. Geophys. Res. **66:**3273–3278.
37. **Seeliger, S., R. Cord-Ruwisch, and B. Schink.** 1998. A periplasmic and extracellular c-type cytochrome of *Geobacter sulfurreducens* acts as a ferric iron reductase and as an electron carrier to other acceptors or to partner bacteria. J. Bacteriol. **180:**3686–3691.
38. **Seki, K., M. Thullner, and P. Baveye.** 2004. Nutrient uptake kinetics of filamentous microorganisms: comparison of cubic, exponential, and Monod models. Ann. Microbiol. **54:**181–188.
39. **Snoeyenbos-West, O. L., K. P. Nevin, R. T. Anderson, and D. R. Lovley.** 2000.

Downloaded from http://aem.asm.org/ on July 24, 2020 at ORTA DOGU TEKNIK UNIVERSITESI

Enrichment of Geobacter species in response to stimulation of Fe(III) reduction in sandy aquifer sediments. Microb. Ecol. **39:**153–167.
40. **Spiteri, C., C. Slomp, K. Tuncay, and C. Meile.** 2008. Modeling biogeochemical processes in subterranean estuaries: the effect of flow dynamics and redox conditions on submarine groundwater discharge of nutrients. Water Resour. Res. doi:10.1029/2007WR006071.
41. **Stelling, J.** 2004. Mathematical models in microbial systems biology. Curr. Opin. Microbiol. **7:**513–518.
42. **Stelling, J., S. Klamt, K. Bettenbrock, S. Schuster, and E. D. Gilles.** 2002. Metabolic network structure determines key aspects of functionality and regulation. Nature **420:**190–193.
43. **Tang, Y. J., R. Chakraborty, H. Garcia Martin, J. Chu, T. C. Hazen, and J. D. Keasling.** 2007. Flux analysis of central metabolic pathways in *Geobacter metallireducens* during reduction of soluble Fe(III)-nitrilotriacetic acid. Appl. Environ. Microbiol. **73:**3859–3864.
44. **Thullner, M., P. Regnier, and P. Van Cappellen.** 2007. Modeling microbially induced carbon degradation in redox-stratified subsurface environments: concepts and open questions. Geomicrobiol. J. **24:**139–155.
45. **Tong, A. H. Y., G. Lesage, G. D. Bader, H. M. Ding, H. Xu, X. F. Xin, J. Young, G. F. Berriz, R. L. Brost, M. Chang, Y. Q. Chen, X. Cheng, G. Chua, H. Friesen, D. S. Goldberg, J. Haynes, C. Humphries, G. He, S. Hussein, L. Z. Ke, N. Krogan, Z. J. Li, J. N. Levinson, H. Lu, P. Menard, C. Munyana, A. B. Parsons, O. Ryan, R. Tonikian, T. Roberts, A. M. Sdicu, J. Shapiro, B. Sheikh, B. Suter, S. L. Wong, L. V. Zhang, H. W. Zhu, C. G. Burd, S. Munro, C. Sander, J. Rine, J. Greenblatt, M. Peter, A. Bretscher, G. Bell, F. P. Roth, G. W. Brown, B. Andrews, H. Bussey, and C. Boone.** 2004. Global mapping of the yeast genetic interaction network. Science **303:**808–813.
46. **Vandevivere, P., and P. Baveye.** 1992. Saturated hydraulic conductivity reduction caused by aerobic-bacteria in sand columns. Soil Sci. Soc. Am. J. **56:**1–13.
47. **Walsh, K., and D. E. Koshland.** 1984. Determination of flux through the branch point of 2 metabolic cycles—the tricarboxylic-acid cycle and the glyoxylate shunt. J. Biol. Chem. **259:**9646–9654.
48. **Watson, I. A., S. E. Oswald, K. U. Mayer, W. Youxian, and S. A. Banwart.** 2003. Modeling kinetic processes controlling hydrogen and acetate concentrations in an aquifer-derived microcosm. Environ. Sci. Technol. **37:**3910–3919.
49. **Weiss, J. V., and I. M. Cozzarelli.** 2008. Biodegradation in contaminated aquifers: incorporating microbial/molecular methods. Ground Water **46:**305–322.
50. **Weitzke, E. L., and P. J. Ortoleva.** 2003. Simulating cellular dynamics through a coupled transcription, translation, metabolic model. Comput. Biol. Chem. **27:**469–481.
51. **Wilkins, M. J., F. R. Livens, D. J. Vaughan, and J. R. Lloyd.** 2006. The impact of Fe(III)-reducing bacteria on uranium mobility. Biogeochemistry **78:**125–150.

Downloaded from http://aem.asm.org/ on July 24, 2020 at ORTA DOGU TEKNIK UNIVERSITESI